ACS APPLIED MATERIALS & INTERFACES

www.acsami.org

Research Article

Role of Zeolite Structural Properties toward Iodine Capture: A Head-to-head Evaluation of Framework Type and Chemical Composition

Brian J. Riley,* Saehwa Chong, Julian Schmid, José Marcial, Emily T. Nienhuis, Mrinal K. Bera, Sungsik Lee, Nathan L. Canfield, Sungmin Kim, Miroslaw A. Derewinski,* and Radha Kishan Motkuri*

Cite This: *ACS Appl. Mater. Interfaces* 2022, 14, 18439–18452

Read Online

ACCESS | Metrics & More | Article Recommendations | Supporting Information

ABSTRACT: This study evaluated zeolite-based sorbents for iodine gas [$I_{2(g)}$] capture. Based on the framework structures and porosities, five zeolites, including two faujasite (FAU), one ZSM-5 (MFI), one mesoMFI, one ZSM-22 (TON), as well as two mesoporous materials, were evaluated for $I_{2(g)}$ capture at room temperature and 150 °C in an iodine-saturated environment. From these preliminary studies, the three best-performing zeolites were ion-exchanged with Ag^+ and evaluated for $I_{2(g)}$ capture under similar conditions. Energy-dispersive X-ray spectroscopy data suggest that Ag-FAU frameworks were the materials with the highest capacity for $I_{2(g)}$ in this study, showing ~3× higher adsorption compared to Ag-mordenite (Ag-MOR) at room temperature, but X-ray diffraction measurements show that the faujasite structure collapsed during the adsorption studies because of dealumination. The Ag-MFI zeolites are decent sorbents in real-life applications, showing both good sorption capacities and higher stability. In-depth analyses and characterizations, including synchrotron X-ray absorption spectroscopy, revealed the influence of structural and chemical properties of zeolites on the performance for iodine adsorption from the gas phase.

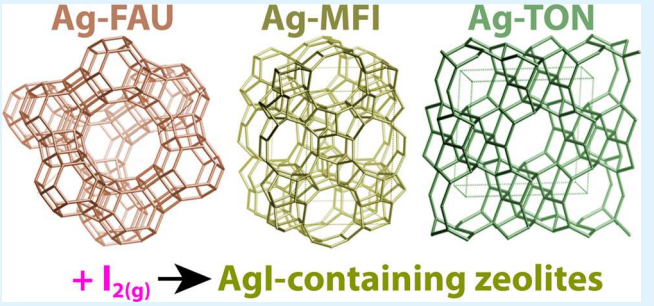

KEYWORDS: *aluminosilicate zeolites, iodine, adsorption, porosity, framework type, X-ray absorption spectroscopy*

INTRODUCTION

Different radioisotopes and compounds of iodine with a range of half-lives ($t_{1/2}$) are released during the reprocessing of used nuclear fuel and in nuclear accidents, including I-131 (^{131}I, $t_{1/2}$ = 8.02 d) and I-129 (^{129}I, $t_{1/2} = 1.57 \times 10^7$ y).[1] Radioiodine can be released into the air and into nearby water sources, facilitating its travel over large distances and incorporation into the human body.[2] Once incorporated, radioiodine can be absorbed in potentially high amounts by the thyroid gland, where it is known to cause thyroid cancer.[3,4] Thus, measures must be taken to avoid the release of radioiodine into the environment.

Generally, on-site implemented sorbent-based approaches have the potential to prevent the release of radioiodine from these sources. Examples of sorbents that can be used to mitigate radioiodine release are metal−organic frameworks (MOFs),[5,6] covalent organic frameworks (COFs),[7] zeolites and mesoporous silica,[8−12] metal-functionalized aerogels or xerogels,[13−16] and other metal-functionalized porous substrates.[17,18] These nanoporous materials have been shown to capture and separate various types of gases.[19−25] For example, zeolites exhibit stability under various conditions such as elevated temperatures, humidity, radiation fluxes, and exposures to different oxidizers [e.g., $NO_{x(g)}$]. Therefore, they are suitable materials to withstand severe conditions that are highly likely to occur during nuclear accidents. Furthermore, since the 1970s, many studies have reported the outstanding ability of zeolites, and especially Ag-exchanged zeolites, to trap different types of volatile iodine species, including $I_{2(g)}$ and CH_3I.[10] Finally, the production processes for making many types of zeolites in large quantities at low costs are at reasonably high technology readiness levels, making their implementation for large-scale industrial applications more suitable than less mature technologies.

This study provides further insights into the influence of zeolite structural and chemical properties on $I_{2(g)}$ adsorption performance. Zeolites are a class of porous ceramic materials composed of structural building blocks, including cages (e.g., α, β, and ε), channels, secondary units, and composite units (see Figure 1 for example structures). Commonly, zeolites are constructed from aluminosilicate frameworks, but other non-aluminosilicate compositions have also been demonstrated in the literature.[26] These materials are connected through an

Received: January 19, 2022
Accepted: March 29, 2022
Published: April 12, 2022

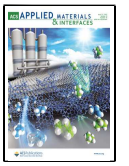

https://doi.org/10.1021/acsami.2c01179
ACS Appl. Mater. Interfaces 2022, 14, 18439−18452

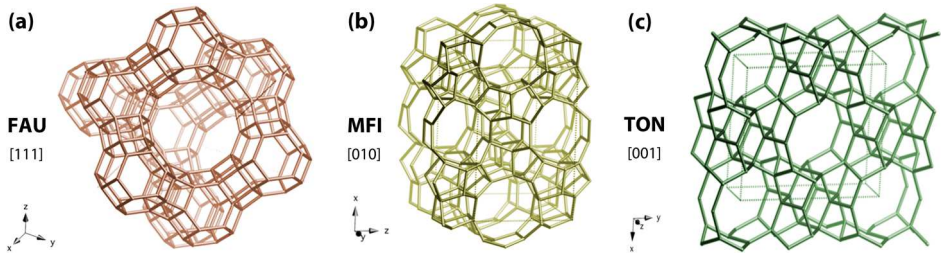

Figure 1. Crystal structure schematics for (a) FAU, (b) MFI, and (c) TON with orientations shown for each. Reprinted (in part) with permission from Baerlocher et al.[26] Copyright 2007 Elsevier.

open network of corner-shared tetrahedra (e.g., SiO_4^{4-} and AlO_4^{5-}) with charge balancing provided to the negatively charged framework by cations (e.g., Na^+ and Ca^{2+}). Zeolites have a wide range of applications, including molecular sieving, water softening, catalysis, carbon capture, and separations.[27−30] Zeolites have also been used to remove a range of radioactive contaminants from aqueous or gaseous streams or for immobilizing nuclear wastes in waste forms.[31−36]

Over the past several decades, metal-exchanged zeolites have been evaluated for $I_{2(g)}$ capture where the base charge balance cations have been exchanged with metals such as Ag, Cd, Cu, Hg, Mn, Pb, Pd, or Tl.[37−39] To date, it appears that Ag remains to be one of the most effective metals for $I_{2(g)}$ adsorption, which is why it was selected for the sorbents in the current study. The current work focused on first capturing $I_{2(g)}$ using base zeolites (not metal-exchanged) followed by an assessment of some Ag-exchanged zeolites to assess the improvements to iodine capture when Ag^+ was included in the zeolite sorbents.

The complexation between iodine and Ag^0 or Ag^+ results in the formation of AgI through a chemisorption process. This process has been well studied in the literature for $I_{2(g)}$ and/or $CH_3I_{(g)}$ capture, especially with zeolites.[9,40−42] One of the benefits of working with Ag as the adsorbing metal is that it is less sensitive to oxidation than other less noble adsorbing metals. Silver is not entirely resistant to oxidation, and it will tarnish in air with a slightly negative Gibbs free energy of formation ($\Delta G_f^\circ = -11.28$ kJ mol^{-1}) shown in reaction 1.[43] The ΔG_f° for AgI formation through a reaction of Ag^0 with I_2 is more spontaneous ($\Delta G_f^\circ = -66.270$ kJ mol^{-1}), as shown in reaction 2,[44] which means that this reaction is favored over the production of Ag_2O (note that in these reactions, "c", "l", and "g" denote crystal, liquid, and gas, respectively).

$$2Ag_{(c)} + 0.5O_{2(g)} \rightarrow Ag_2O_{(c)} \quad (\Delta G_f^\circ = -11.28 \text{ kJ mol}^{-1} \text{ at } 298.15 \text{ K}) \tag{1}$$

$$Ag_{(c)} + 0.5I_{2(c,l,g)} \rightarrow AgI_{(c,l)} \quad (\Delta G_f^\circ = -66.270 \text{ kJ mol}^{-1} \text{ at } 298.15 \text{ K}) \tag{2}$$

In a recent study evaluating various adsorbing metals for $I_{2(g)}$ in aluminosilicate gel scaffolds,[45] thermodynamic calculations were made with additional cationic adsorbents including Sb^{3+}, Sn^{2+}, and Sn^{4+}, where metal-iodide and metal-oxide formations were compared. This type of comparison revealed a few metal options that showed the preference for metal-iodide formation over metal-oxide formation within (at least a portion of) the temperature range of 25 °C ≤ T ≤ 500 °C including Ag^+, Ba^{2+}, Cs^+, Eu^{2+}, Hg^+, Hg^{2+}, K^+, Pb^{2+}, Pd^{2+}, Pt^{2+}, Pt^{4+}, Rb^+, Sr^{2+}, and Tl^+. Some of these are not likely to be good choices as adsorption sites due to environmental toxicity (e.g., Ba, Hg, and Pb) or cost (e.g., Pd and Pt), and Ag seemed to rise to the top of the list again with preference to AgI formation over Ag_2O formation across this entire temperature range. Older studies by Maeck et al.[46] and Jubin[42] provide some background information on early work looking at metal-exchanged zeolites for either $I_{2(g)}$ or $CH_3I_{(g)}$ capture. The report by Jubin[42] provides a wealth of references for various types of testing and operational behaviors with metal-exchanged zeolites (e.g., Ag and other metals) including poisoning, regeneration, temperature cycling, humidity, aging, radiation effects, particle size, as well as many other variables.

Zeolites with higher SiO_2/Al_2O_3 molar ratios are more acid-resistant but tend to have lower capacities for ion exchange.[47,48] Thus, zeolites like mordenite (i.e., $SiO_2/Al_2O_3 \sim 10$) are expected to have better long-term durability within the acidic environment in an off-gas facility for reprocessing used nuclear fuel than zeolites like faujasite (FAU, i.e., $SiO_2/Al_2O_3 \sim 2.48$) or Linde 4A (i.e., $SiO_2/Al_2O_3 \sim 1.92$). It is this topic of acid resistance that resulted in silver mordenite (i.e., Ag-MOR) being selected as a better candidate for use as the baseline iodine sorbent for reprocessing facilities, and that is why it is included in this study as a point of comparison. However, Ag-FAU shows a much higher iodine capacity as reported by Maeck et al.[46] compared to Ag-MOR, making it eligible as a potential alternate candidate sorbent for iodine capture at different operating temperatures or under less acidic off-gas conditions.

In this paper, we investigated the different performances of zeolites for iodine adsorption based on their physicochemical properties, such as geometry (i.e., 10-membered rings vs 12-membered rings and supercages), dimensionality of the porous framework (i.e., 1-dimensional framework vs 3-dimensional framework), chemical composition (i.e., Si/Al ratio and Ag), and pore size (i.e., micropores vs mesopores). The materials selected for this work were FAU, ZSM-5 (MFI), mesoMFI, ZSM-22 (TON), and two mesoporous silicates (i.e., SBA-15 and Al-SBA-15). The FAU-type zeolites are characterized by a three-dimensional framework consisting of ∼1.2 nm large supercages interconnected with 12-member ring channels measuring 0.74 nm in diameter. The MFI-type zeolites (i.e., ZSM-5) likewise have a tridimensional microporous system and 10-member ring channels with Ø 0.51 × 0.55 nm and Ø 0.53 × 0.56 nm pore sizes. The mesoMFI-type zeolites (i.e., MFI-type) are MFI nanocrystals (ca. 30−40 nm) aggregated into larger blocks where intercrystalline mesopores are present; no intracrystalline mesopores were present in the sample. A unidimensional microporous system distinguishes the TON-type zeolites (i.e., ZSM-22) with 10-member ring channels Ø 0.46 × 0.57 nm. The SBA-15 material is based on uniform hexagonal pores with a narrow pore size distribution and a

https://doi.org/10.1021/acsami.2c01179
ACS Appl. Mater. Interfaces 2022, 14, 18439−18452

tunable pore diameter ranging from 5 to 15 nm. Details about these different materials and some crystal structures are provided in Table S1 (Supporting Information) and Figure 1, respectively.

MATERIALS AND METHODS

Sorbent Syntheses. The synthesis processes followed to create the samples within this study were based on the reported literature for FAU,[49,50] MFI,[51] mesoMFI,[52] TON,[53,54] SBA-15,[55] and Al-SBA-15[56] with detailed procedures provided in the Supporting Information.

Silver-Exchanging of Base Materials (IE×1 and IE×2). Silver-exchanging of base materials was done for FAU, MFI, and TON zeolites using $AgNO_3$ solution on the as-made FAU (sample 2), MFI (sample 6), and TON (sample 20), respectively (see Table S1, Supporting Information). Here, a 1 M $AgNO_3$ solution was prepared in deionized water (DIW) within a darkroom (under red light) to avoid photoreduction of Ag^+ and precipitation of Ag^0. To obtain the Ag-exchanged forms of the zeolites, the ion-exchange procedure was repeated two times, where zeolites were added to 1 M $AgNO_3$ solutions in a 1:20 mass/volume (g/mL) ratio and stirred at 80 °C for 2 h under reflux. After the first ion exchange (IE×1), the preparation was centrifuged and washed with DIW, and then the procedure was repeated under the same conditions (IE×2) for approximately half of the IE×1 sample. The resulting Ag-exchanged zeolites were dried at 80 °C in air overnight.

Activation of Ag-exchanged (IE×1 and IE×2) Zeolites. After the second Ag-exchanging (IE×2), activation of portions of IE×1 and IE×2 zeolites was performed by heating the samples in a vacuum oven at 150 °C overnight in glass vials. After cooling down to room temperature, the samples were removed and inserted into new glass vials for $I_{2(g)}$ uptake experiments immediately thereafter (discussed in a later section). The activation process was performed to improve the sorption performance of the Ag-exchanged zeolites and the vacuum was used to help prevent oxidation of any reduced silver (Ag^0) present.

Iodine Loading of Base Materials at 150 °C. The reason behind the selection of 150 °C is that this is the expected temperature of the solid sorbent off-gas column in a reprocessing facility for used nuclear fuel. At this temperature, the prevalent physical state of iodine is gaseous. Iodine loading was conducted for several different sets of experiments at separate times using the same procedure. For the initial tests, starting masses ($m_{s,i}$) of ~0.1 g of each sample, along with a sample of silver mordenite (Ag-MOR, IONEX Ag-900 from Molecular Products, Louisville, CO; Si/Al = 5:1), were loaded into pre-tared 4-mL glass vials (Qorpak GLC-00980), and these were placed into a 1-L standard perfluoroalkoxy (PFA) jar (100-1000-1, Savillex LLC, Eden Prairie, MN) containing a vial of 0.2 g iodine (99.8%, Sigma-Aldrich). The small sample masses used here were selected for screening the materials. An empty vial was included in the test as a baseline for iodine adsorption on the vessel. The lid was placed on the vessel, and the vessel was loaded into an oven at 150 ± 5 °C for 24 h. Following the 24 h soak, the lid was removed from the Savillex vessel and the samples were placed back into the oven so that any loosely physisorbed iodine could be desorbed, and this process was conducted for 1 h. Then, the samples were directly transferred into a vacuum desiccator to cool overnight. Each sample container was weighed to determine the mass after loading ($m_{s,f}$), and the mass change was determined (Δm). Because the sorbents were not activated prior to the uptake experiments, the mass uptake values were recorded for information only because some samples likely underwent water desorption during the iodine loading procedure.

Iodine Loading in Ag-exchanged Materials at 150 °C. The second iodine uptake experiment was conducted on Ag-exchanged materials using (a) as-exchanged samples and (b) as-exchanged and then activated samples. Here, smaller sample masses (i.e., $m_{s,i}$ ~0.02−0.08 g) were used for sorption testing. Like before, samples were loaded into Qorpak vials and the 1-L Savillex jar. These were left in the oven at 150 ± 5 °C for 24 h, followed by desorption for 1 h in the absence of iodine. Samples were weighed after uptake to determine $m_{s,f}$ and Δm values.

Iodine Loading at Room Temperature. Room temperature $I_{2(g)}$ uptake was also evaluated for the Ag-exchanged (IE×2) samples. Here, the 1-L Savillex jar was loaded with the samples in tared Qorpak vials containing Ag-FAU-IE×2, Ag-MFI-IE×2, Ag-TON-IE×2, and Ag-MOR along with a blank vial and a vial containing iodine crystals (99.999%, Alfa Aesar); the lid was added and these were left at room temperature (~22 ± 3 °C) for 32 days when the mass uptake had seemed to mostly stabilize. Sample masses were recorded at various times until a constant mass uptake was observed. Following the iodine uptake experiment, the glass vial containing iodine was removed from the PFA jar and left in a fume hood at room temperature to allow for any physisorbed iodine to desorb. For desorption, the masses of samples were recorded over 9 days until the masses had stabilized.

Iodine Loading Calculations. Following the iodine loading experiments, eqs 3−5 were used to evaluate the mass changes during the iodine loading experiments where $m_{s,i}$ was the initial sample mass (before loading), $m_{s,f}$ is the final mass (after loading), Δm is the mass change during the experiment after iodine capture, MPD (mass percent of the delta) is the relative mass % change in the loaded sample after loading, and MCR (mass change ratio) is defined as "g g^{-1}" and loosely denotes the mass of iodine captured per starting mass of the sorbent (loading). The MCR values are likely not mass changes due to iodine capture alone because, under the conditions utilized during iodine loading, water adsorption and/or desorption were also possible and could help explain both $+\Delta m$ and $-\Delta m$ values. Finally, the Ag-utilization (AgU) was calculated as the atomic ratio of I/Ag in the iodine-sorbed samples shown in eq 6 using sample concentration data measured with energy-dispersive X-ray spectroscopy (EDS). When AgU > 1, this suggests that some physisorbed iodine remained within the sample after the active desorption step or iodine was binding to a different location within the sorbent than to the metal directly; it is possible that iodine adsorbed directly to the zeolite surfaces.

$$\Delta m = m_{s,f} - m_{s,i} \tag{3}$$

$$\text{MPD} = 100(\Delta m / m_{s,f}) \tag{4}$$

$$\text{MCR} = \Delta m / m_{s,i} \ (\text{or g g}^{-1}) \tag{5}$$

$$\text{AgU} = 100^{*}[\text{I}]/[\text{Ag}] \ (\text{at.\%/at.\%}) \tag{6}$$

Scanning Electron Microscopy and Energy-dispersive X-ray Spectroscopy. Scanning electron microscopy (SEM) was performed with a backscattered electron detector for elemental contrast using a JSM-7001F field emission gun scanning electron microscope (JEOL USA, Inc. Peabody, MA) on samples mounted to aluminum stubs with carbon tape and coated with 2.5 nm of Pt using a Quorum 150T ES (Electron Microscopy Sciences, Hatfield, PA). EDS analyses were performed using a Bruker xFlash 6|60 (Bruker AXS Inc., Madison, WI) using Bruker ESPRIT software for data processing; data collection was conducted at 15 kV acceleration voltage at 40k−60k counts per second.

Powder X-ray Diffraction. Powder X-ray diffraction (P-XRD) analyses were performed on the materials using a Bruker D8 Advance (Bruker AXS Inc., Madison, WI) with a Cu X-ray tube. The detector used was a LynxEye position-sensitive detector with a collection window of 3° 2θ. Scan parameters were 5−70° 2θ with a step of 0.015° 2θ and a 0.3-s dwell at each step. Samples were mounted to a zero-background silicon or quartz holder by suspending the powder in isopropanol and using a drop technique to apply it to the holder. Peak identification and quantification according to the fundamental parameters approach[57] were performed using Bruker AXS DIFFRAC^{plus} EVA (v14) and Bruker AXS Topas (v4.2), respectively. For zeolites without iodine, a Rigaku Miniflex II type XRD was used for analysis with a Cu X-ray tube (30 kV and 15 mA). Each sample was loaded on a quartz holder and then measured in the 2θ range of 3−40° using a step size of 0.02° 2θ with hold times of 1.0 s per step. Diffraction patterns were analyzed with the Rigaku PDXL2 software.

https://doi.org/10.1021/acsami.2c01179
ACS Appl. Mater. Interfaces 2022, 14, 18439−18452

X-ray Absorption Spectroscopy. X-ray absorption spectroscopy (XAS) was performed on three Ag-exchanged samples (i.e., Ag-FAU-IE×2, Ag-MFI-IE×2, and Ag-TON-IE×2), three iodine-loaded samples (i.e., AgI-FAU-IE×2-150, AgI-MFI-IE×2-150, and AgI-TON-IE×2-150), and three standards (i.e., AgI, Ag_2O, and Ag foil) near the Ag K-edge (25.514 keV) at the Advanced Photon Source (APS) at Argonne National Laboratory utilizing beamline 12-BM-B operated in top-up mode using a Si(111) monochromator and calibrated using Ag foil. One additional standard (i.e., $AgNO_3$) was measured at APS beamline 15-ID-D (NSF's ChemMatCARS) also operated in top-up mode with a Si(111) monochromator. Approximately 5−10 mg of sample powders and standards were mixed (separately) with ∼20 mg of boron nitride binder and pressed into 7 mm diameter pellets at 70 MPa using a uniaxial press. Sample pellets were placed between pieces of polyimide (Kapton) tape. The step sizes were 5.0 eV (for the energy range of 25.314−25.499 keV), 0.6 eV (for 25.499−25.544 keV), and between 0.05/Å (for 25.545−26.369 keV). The XAS data were normalized using ATHENA software.[58] The primary focus of interest was the X-ray absorption near edge structure (XANES) portion (i.e., 25.499−25.544 keV) of the absorption spectra.

RESULTS AND DISCUSSION

The gravimetric data for the $I_{2(g)}$ capture with as-made (not Ag-exchanged) zeolites including $m_{s,i}$, $m_{s,f}$, Δm, and MPD values as well as the mass % of iodine measured with EDS ($m_{I,EDS}$, excluding oxygen) are presented in Table S2 (Supporting Information). Pictures of the samples before and after iodine loading are shown in Figure S1 (Supporting Information). Additionally, from these data, it was apparent that several samples showed iodine capture, despite not having active metallic sites for iodine chemisorption, as was the case for Ag-MOR to form AgI. Also, the mass % uptake (MCR or $\Delta m/m_{s,i}$) did not correspond to the mass of iodine present in the sample as measured with EDS ($m_{I,EDS}$), possibly due to variable amounts of water bound in the zeolite that was desorbed during the iodine loading procedure at 150 ± 5 °C. For that reason, EDS data were only utilized for the down selection of the zeolites for the subsequent steps, including Ag exchange and additional iodine testing.

These data showed promise that some of these zeolites could be used to capture iodine without any metal functionalization, preventing additional processes like metal loading and the use of toxic metals such as Ag for capturing the $I_{2(g)}$. Because the iodine did not desorb during the bake-out procedure directly after the iodine loading for some of the base samples, it is uncertain how tightly bound the iodine was in these zeolites. Based on these initial adsorption data for the base sorbents, three framework structures of FAU (sample 2), MFI (sample 6), and TON (sample 20) were selected for subsequent testing (see Table S2, Supporting Information). The base mesoMFI, SBA-15, and Al-SBA-15 showed very small sorption ($m_{I,EDS}$ and MPD) values (∼0.5 mass %), but their iodine capture performances could likely be improved if functionalized with metal cations (e.g., Bi^{3+} and Ag^+) targeted for this purpose.[59]

Pictures of FAU, MFI, and TON zeolites including as-made, Ag-exchanged (IE×1), Ag-exchanged after $I_{2(g)}$ loading at 150 °C, and activated Ag-exchanged (IE×2) after $I_{2(g)}$ loading at 150 °C are provided in Figure 2. Distinct changes were observed in the appearances of the different materials during the Ag-exchange and the iodine adsorption steps despite nearly identical light-colored starting appearance as depicted in Figure 2. These changes represent different chemical phenomena occurring within the zeolites. After the Ag-exchange (IE×2) process, the Ag-FAU-IE×2 sample was very dark brown, while Ag-MFI-IE×2 and Ag-TON-IE×2 remained similar in color to the as-made zeolites, albeit with slightly darker appearances. While the color of Ag-exchanged FAU changed to bright yellow during $I_{2(g)}$ adsorption, the corresponding MFI and TON samples appeared red and brown, respectively. The dark color of Ag-FAU should be directly correlated with a high Ag loading as a result of high Al content in the FAU zeolite [Si/Al = 1.1, ca., 90 Al per unit cell (T = 192)]. Subsequent formation of brown-black silver oxide (Ag_2O) species/clusters in Ag^+-exchanged material seems to be responsible for the observed color change. The commercial Al-rich Ag-MOR (IONEX Ag-900) sample used for I_2 loading has a color similar to that of the Ag-FAU (Si/Al = 1.1) sample; see Riley et al.[13] for a picture of these sorbents.

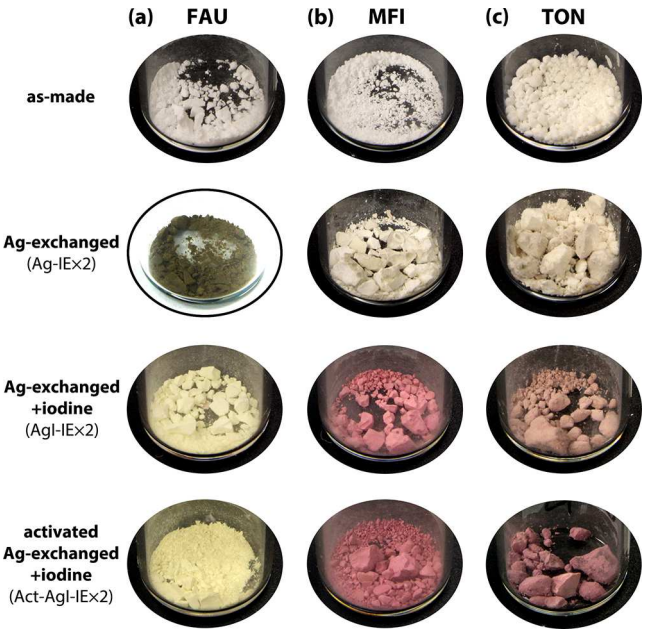

Figure 2. Collage of pictures of (a) FAU, (b) MFI, and (c) TON zeolites as-made after the second Ag-exchange (IE×2), iodine-loaded Ag-exchanged (IE×2), and iodine-loaded IE×2 after activation. Iodine-loaded samples were loaded at 150 °C. Pictures were taken of the samples within Qorpak vials.

In the cases of MFI and TON zeolites, which contain much less Al, that is, Si/Al = 26 and 31, respectively (ca. 3.5 and 2 Al atoms per unit cell), where the unit cells contain 96 and 64 T (Si, Al) atoms for MFI and TON, respectively, the ion-exchange procedure results in a significantly lower Ag^+ content. Moreover, larger distances between the dispersed Ag^+ reduced the possibility of silver oxide cluster formation. Thus, low Ag content and limited (if any) formation of nanoclusters are responsible for the (almost) unchanged color of Ag-MFI and Ag-TON in comparison to the parent zeolites, and the original structures were well maintained as per P-XRD analyses (Figure S9, Supporting Information).

This may indicate at least some molecular iodine occluded on the surface (e.g., at pore openings) and/or in the subsurface layer of the MFI and TON crystals. In both zeolites, the smaller size of 10MR (in comparison to 12MR windows connecting supercages in FAU) decreases the rate of diffusion during the active desorption process implemented after the iodine loading procedure to remove loosely physisorbed iodine. Besides, the additional interaction between iodine

https://doi.org/10.1021/acsami.2c01179
ACS Appl. Mater. Interfaces 2022, 14, 18439−18452

Table 1. Mass Uptake and EDS Data for $I_{2(g)}$ Capture of Ag-exchanged Zeolites after Exposures at 150 °C, Including Both Unactivated and Activated Sorbents[a]

sample type	$m_{s,i}$ (g)	Δm (g)[b]	MPD (mass %)	MCR (g g^{-1})	$m_{I,EDS}$ (mass %)	$M_{Ag,EDS}$ (at. %)	$M_{I,EDS}$ (at. %)	AgU
AgI-MOR-150(1)	0.1057	0.0098	8.5%	0.093	19.8 (0.2)	5.0 (0.12)	6.0 (0.07)	1.19 (0.04)
AgI-MOR-150(2)	0.0392	0.0038	8.8%	0.10	25.9 (0.3)	7.9 (0.22)	8.8 (0.16)	1.11 (0.01)
AgI-FAU-IE×1-150	0.0422	0.0046	9.8%	0.11	29.1 (0.6)	21.4 (0.3)	13.3 (0.3)	0.62 (0.02)
AgI-FAU-IE×2-150	0.0567	0.0080	12.4%	0.14	29.0 (1.8)	22.5 (0.7)	13.5 (0.9)	0.60 (0.06)
AgI-MFI-IE×1-150	0.0770	0.0078	9.2%	0.10	7.1 (0.6)	1.6 (0.1)	1.7 (0.2)	1.09 (0.06)
AgI-MFI-IE×2-150	0.0603	0.0051	7.8%	0.085	8.4 (0.6)	1.8 (0.01)	2.1 (0.2)	1.13 (0.09)
AgI-TON-IE×1-150	0.0293	−0.0006	−2.1%	−0.020	9.4 (0.9)	1.7 (0.1)	2.4 (0.3)	1.41 (0.10)
AgI-TON-IE×2-150	0.0204	−0.0005	−2.5%	−0.025	11.4 (0.6)	2.0 (0.03)	2.9 (0.2)	1.45 (0.08)
Act-AgI-FAU-IE×1-150	0.0270	0.0102	27.4%	0.38	36.1 (1.4)	18.8 (0.1)	16.9 (0.9)	0.90 (0.05)
Act-AgI-FAU-IE×2-150	0.0341	0.0098	22.3%	0.29	32.3 (0.4)	20.1 (0.6)	14.9 (0.4)	0.74 (0.01)
Act-AgI-MFI-IE×1-150	0.0450	0.0042	8.5%	0.093	8.8 (0.1)	1.9 (0.1)	2.2 (0.04)	1.13 (0.03)
Act-AgI-MFI-IE×2-150	0.0565	0.0069	10.9%	0.12	8.4 (1.2)	1.6 (0.1)	2.1 (0.3)	1.29 (0.11)
Act-AgI-TON-IE×1-150	0.0199	0.0005	2.5%	0.025	15.0 (0.6)	1.9 (0.1)	4.0 (0.2)	2.05 (0.08)
Act-AgI-TON-IE×2-150	0.0271	0.0009	3.2%	0.033	13.8 (0.2)	2.3 (0.1)	3.6 (0.1)	1.61 (0.07)

[a]Data reported here include the initial sample masses ($m_{s,i}$), the mass changes during iodine loading (Δm), the MPD (mass percent of delta; $100{\cdot}\Delta m/m_{s,f}$) values, the MCR values, the mass % of iodine measured in the samples with EDS ($m_{I,EDS}$), the at. % of Ag measured in the sample with EDS ($M_{Ag,EDS}$), the at. % of I measured in the sample with EDS ($M_{I,EDS}$), and AgU values. Note that EDS data exclude oxygen. Values in parenthesis are standard deviations ($\pm 1\sigma$) from multiple measurements. See eqs 3−6 for more information regarding the terms. [b]Note that this accounts for water uptake as well as iodine uptake.

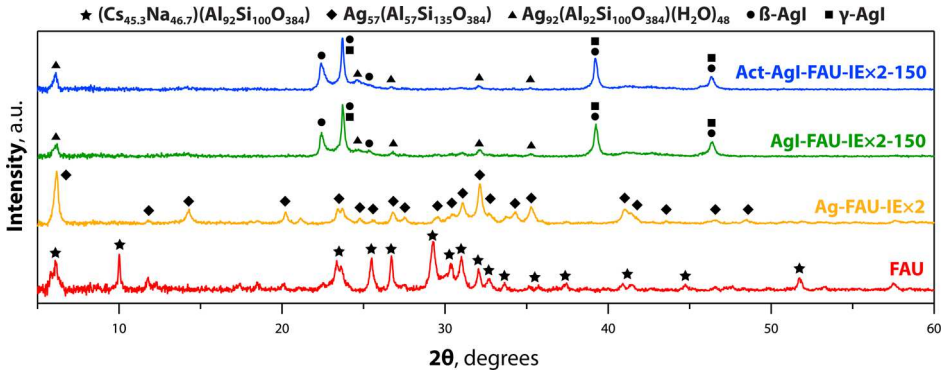

Figure 3. P-XRD of FAU samples including FAU (as-made), Ag-FAU-IE×2, AgI-FAU-IE×2-150, and Act-AgI-FAU-IE×2-150. See the text for sample descriptions.

molecules and charge-bearing Ag^+ and/or other cations species in the framework could slow down the kinetics of the removal of iodine molecules from the zeolites. In addition, the presence of dispersed AgI species in zeolite channels also generates an additional barrier for diffusion (removal) of I_2 molecules occluded/trapped in micropores. Such behavior should be more distinct in the case of unidirectional TON than tridimensional MFI. As a result, there is a much more heterogeneous distribution of iodine in the crystal body and strong enrichment of iodine in the surface/subsurface layer. In the case of the tridimensional MFI zeolite, one could expect a smaller extent of a similar process because of less hindered diffusion of iodine molecules from the channels and as a result, less iodine uptake was observed in Ag-MFI.

In the case of the iodine-loaded Ag-FAU framework system, the light-yellow color of the sample suggests that it contains no free iodine, at least on the surface or in the subsurface layer, but rather, the iodine present is purely in the form of crystalline AgI, which is of deep yellow color. This can be caused by the chemical bonding of iodine and structural transformation of FAU occurring during $I_{2(g)}$ sorption at 150 °C through chemisorption to form AgI.

Iodine uptake data for 150 °C for the Ag-exchanged FAU, MFI, and TON zeolite samples are provided in Table 1, including IE×1 and IE×2 before and after activation. For the FAU and TON samples, the Ag-exchanged zeolites and activated Ag-exchanged zeolites performed better for capturing $I_{2(g)}$ at 150 °C than the unfunctionalized zeolites. Ag-FAU and, to a significantly lower extent, Ag-MFI and Ag-TON formed AgI phases when exposed to iodine according to the P-XRD data (Figures S2−S8, Supporting Information), showing the chemisorption of iodine into these samples. The gravimetric iodine loading results showed that the Act-AgI-FAU-IE×1 had the highest iodine loading of 38 mass %. Compared to 4−6 mass % iodine uptake on the as-made FAU zeolite without Ag, the iodine loading substantially increased after Ag was added to the FAU zeolite. It is worth noting that while the $m_{I,EDS}$ values were similar between the activated and unactivated Ag-zeolites, the gravimetric data (i.e., MPD and MCR) between these data sets were notably different. This is likely due to water adsorption from the atmosphere during iodine loading experiments for activated zeolites. The activated Ag-MFI zeolites showed 8−9 mass % of iodine loading, and the activated Ag-TON zeolites showed 14−15% of iodine loading because of surface/subsurface loading of iodine as discussed

https://doi.org/10.1021/acsami.2c01179
ACS Appl. Mater. Interfaces 2022, 14, 18439−18452

earlier. In general, the activated zeolites showed higher iodine loading than unactivated zeolites. Because EDS is a technique for surface and shallow-subsurface layer analysis, it might not reflect the real iodine concentrations in these samples.

The P-XRD data for both AgI-FAU-IE×1-150 and Act-AgI-FAU-IE×1-150 showed AgI (β, γ) phases with some small intensity peaks, possibly from $Ag_{92}(Al_{92}Si_{100}O_{384})$ $(H_2O)_{48}$ (PDF 01-071-6663)—see Figures S2 and S3 (Supporting Information). These do not show FAU peaks, which is likely due to the decomposition of the FAU crystal structure during the iodine uptake process at 150 °C. Both AgI-MFI-IE×1-150 and AgI-MFI-IE×2-150 showed low-intensity reflections attributed to γ-AgI as well as to $H_{1.22}(Si_{94.43}Al_{1.57}O_{192})$ $(H_2O)_{16}$, that is, evidence of the preserved MFI structure (PDF 01-079-1638)—see Figures S6 and S7 (Supporting Information). The Act-AgI-TON-IE×2-150 sample showed potential fits for AgI phases after the 150 °C $I_{2(g)}$ exposure, but confirmation was difficult based on the weak diffraction peaks and this is likely due to the limited quantity of iodine present (see Figure S8, Supporting Information). A summary of diffraction patterns for FAU samples at different stages of sorbent development is shown in Figure 3.

Some SEM micrographs of selected zeolites after the 150 °C $I_{2(g)}$ uptake experiments are provided in Figure 4, and others are provided in the Supporting Information (see Figures S9–S11). These all show discrete geometric shapes, as are often observed with zeolites. The EDS results show that Act-AgI-FAU-IE×1 had the highest iodine loading of 36.1 mass % ($m_{I,EDS}$), which was higher than the gravimetric iodine uptake of 27.4 mass % ($100 \times \Delta m/m_{s,f}$ or MPD; see Table 1). The depth of the penetration of electrons during EDS analysis depends on the density of the material, which changes for the zeolites; other variables affect this as well, like the acceleration voltage of the electron beam used during EDS analysis (i.e., 15 kV for these samples). In this study, the density of the material increased from FAU (12.7 T/1000 Å^3) to MFI (17.9 T/1000 Å^3) to TON (19.7 T/1000 Å^3). In the case of Ag-TON, the disagreement between gravimetric and EDS data suggests that most of the iodine was located in the surface and subsurface layers of the crystallites, which can be ascribed to the slower diffusion of iodine through the unidirectional pore system of TON.

The Act-Ag-FAU zeolites showed ~4× the iodine capacity of equivalent Act-Ag-MFI zeolites and 2.5× the iodine capacity of Act-Ag-TON zeolites (i.e., based on $m_{I,EDS}$ data—see Table 1). Both gravimetric and EDS analyses show that Ag-FAU zeolites had a higher capability to bind I_2 than Ag-MFI and Ag-TON zeolites but with less structural stability based on the P-XRD data mentioned previously. Between Ag-MFI and Ag-TON, Ag-MFI had higher iodine loading in gravimetric measurements, whereas Ag-TON showed higher loading in EDS analysis, which is attributed to the surface measurement only utilized for EDS discussed previously. The discrepancy here for TON samples where MPD $\ll m_{I,EDS}$ could also be due to water desorption during the iodine loading procedure. Nevertheless, more silicious MFI (Si/Al = 26) and TON (Si/Al = 31) are significantly more stable than Al-rich FAU (Si/Al = 2.2). Elemental analysis showed no change in the Si/Al ratios (in the range of measurement accuracy) for the parent and iodine-loaded MFI and TON samples, respectively. Also, because of the presence of a large amount of Al in FAU and a large number of ion-exchangeable sites, a large amount of Ag is introduced during Ag-exchange, and the adsorbed iodine is in the form of AgI (see Figure 3 as well as Figures S3–S5, Supporting Information), which gives these samples their distinct yellow color. Further, the open framework due to microporosity eliminated during $I_{2(g)}$ sorption at 150 °C for a prolonged time will help remove the physisorbed and weekly bonded molecular iodine. As mentioned previously, when looking at the P-XRD data for the iodine-loaded and activated TON sample, Act-AgI-TON-IE×2-150, the presence of AgI phases was inconclusive (see Figure S8, Supporting Information).

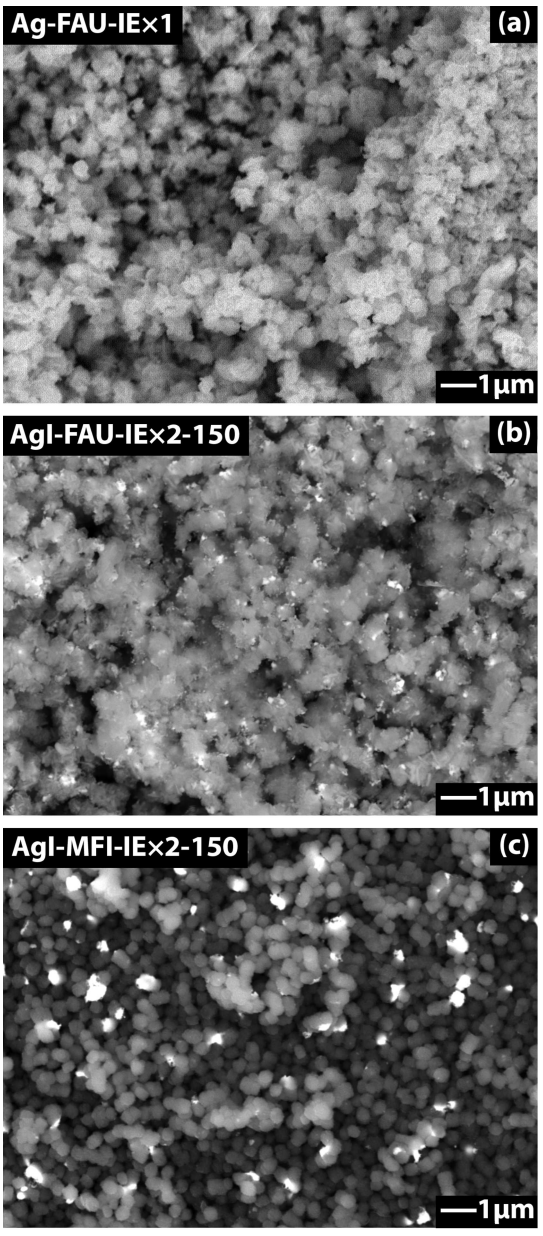

Figure 4. SEM micrographs of (a) Ag-FAU-IE×1, (b) AgI-FAU-IE×2-150, and (c) AgI-MFI-IE×2-150.

In the case of both MFI and TON, the small amounts of Al in these zeolite frameworks (i.e., Si/Al = 26 and 31, respectively) result in fewer numbers of ion-exchangeable sites; thereby, only small amounts of Ag are introduced in these frameworks during the Ag-exchange process. The AgI formed during the sorption is highly dispersed and in a small amount (see Figures 2 and S6–S8, Supporting Information).

https://doi.org/10.1021/acsami.2c01179
ACS Appl. Mater. Interfaces 2022, 14, 18439–18452

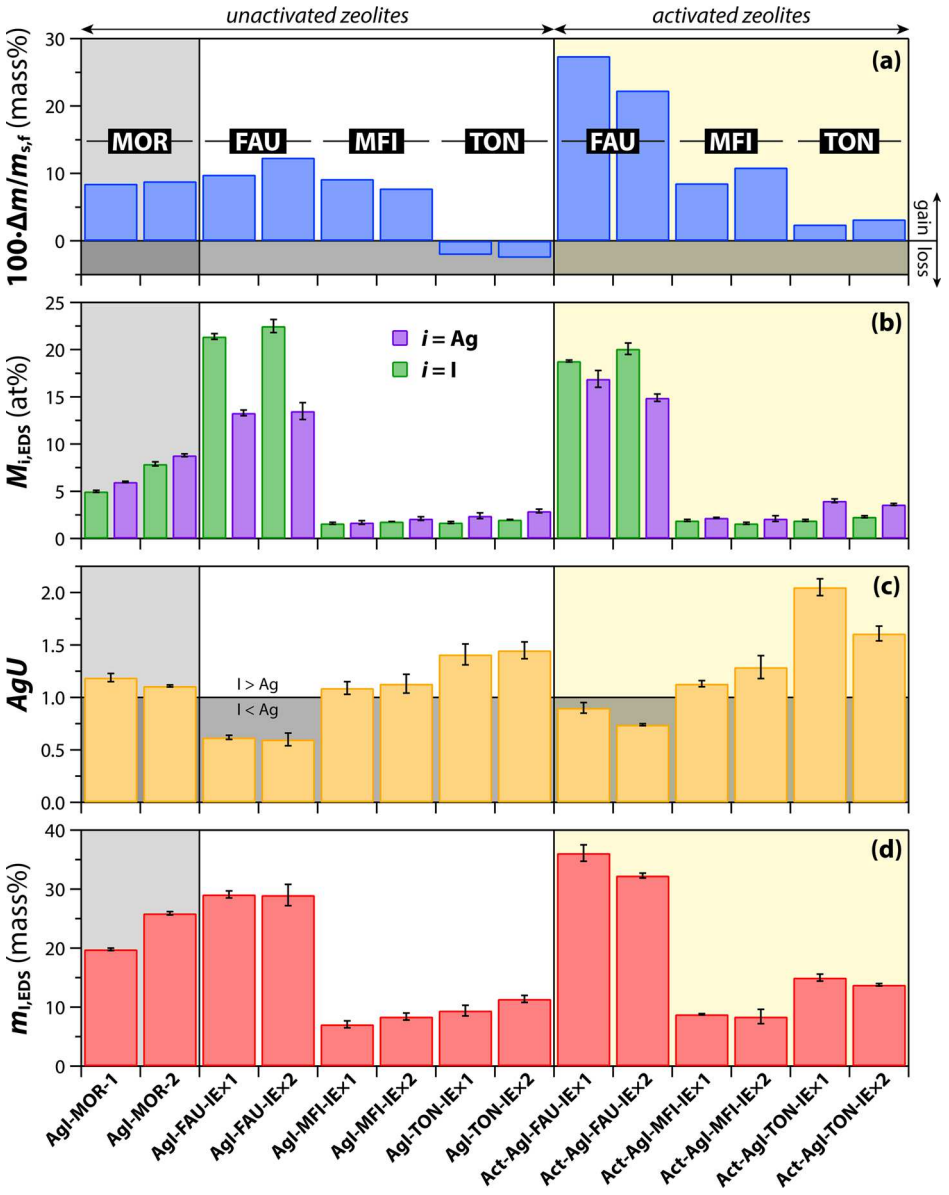

Figure 5. Summary of data for unactivated zeolites (including two data points for Ag-MOR) and activated zeolites including (a) $100{\cdot}\Delta m/m_{s,f}$ (mass %) (also called MPD), (b) $M_{i,EDS}$ (i = Ag and I; at. %), (c) AgU (at. %), and (d) $m_{I,EDS}$ (mass %). These data are for samples $I_{2(g)}$-loaded at 150 °C. Note that the data in (b–d) exclude oxygen during quantification.

The main form of iodine detected in the MFI and TON zeolites is likely molecular I_2 (interacting with local charges in the framework) and is probably occluded in the 10MR channels. Also, the iodine present on the MFI and TON samples appears to be either tightly physisorbed or possibly even chemisorbed to the zeolite framework considering that it did not desorb during that final step of the iodine-loading process. It is also possible that a longer time is required to equilibrate the system. The short time of the desorption process does not remove all occluded I_2 molecules from the pores and, therefore, reveals enrichment in I_2 on the subsurface layers of the crystals. Thus, this limited the use of EDS to determine the iodine content to the fullest extent possible. More distinct effects of the surface/subsurface of crystal enrichment in MFI and TON crystals are because of slightly smaller channels, the unidimensional pore systems (hindered diffusion of I_2 molecules), and lower numbers of active sites (Si/Al = 26 or 31), respectively.

A summary of the data from the 150 °C experiment is shown graphically in Figure 5. These comparisons accentuate the differences in performance between the Ag-FAU, Ag-MFI, and Ag-TON samples from different preparation stages where the FAU sorbents performed exceptionally better in terms of iodine uptake. The AgU values for Ag-MFI and Ag-TON are >1 because of the presence of iodine molecules trapped in the channels of the 10MR micropore system and not directly tied to Ag utilization through AgI formation. In looking at the data presented in Figure 5c (AgU) and Figure 5d ($m_{I,EDS}$) together, it is apparent that the activation processes utilized prior to iodine loading improved iodine loadings in these samples over unactivated samples, albeit by slight amounts. Also, the differences between activated and unactivated zeolites based on mass changes (i.e., $\Delta m/m_{s,f}$, Figure 5a) show that the activated zeolites generally took up more mass during the iodine loading experiment. This is likely due to the removal of adsorbed water from the zeolites during activation so that the

https://doi.org/10.1021/acsami.2c01179
ACS Appl. Mater. Interfaces 2022, 14, 18439–18452

initial sample masses were more representative of low-moisture or moisture-free sample masses.

In looking at the XANES data collected from APS, linear combination fittings of the raw data using standards of Ag-MOR, Ag foil, Ag_2O, and AgI were performed to estimate silver valence states in Ag-FAU-IE×2, Ag-MFI-IE×2, Ag-TON-IE×2, AgI-FAU-IE×2-150, AgI-MFI-IE×2-150, and AgI-TON-IE×2-150. To do the fitting, eq 7 was used where Ag_{calc} is the calculated Ag K-edge spectrum from a given sample, x_i is the mole fraction of component i, and A_i is the measured Ag K-edge spectrum of standard i, where i represents Ag metal (Ag^0), AgI, Ag_2O, or Ag-MOR. Data for Ag-MOR were obtained from the report by Abney et al.[60] to represent the environment of Ag in a general zeolite material; while this will vary between different types of zeolite, it was used as a starting point.

$$Ag_{Calc} = \sum_{i=1}^{n} x_i A_i \tag{7}$$

Table 2 lists the fitted mole fractions of the components, that is, Ag^0, Ag_2O, Ag-MOR, and AgI. Based on these fits, the

Table 2. Linear Combination Fitting Results for Ag K-edge XANES of Zeolite Samples [i.e., x_i Values from Equation 7]

sample name	Ag^0	Ag_2O	Ag-MOR	AgI	Ag^0/Ag^+
Ag-FAU-IE×2	0.215	0.122	0.663	0.000	0.274
AgI-FAU-IE×2-150	0.000	0.000	0.180	0.820	-
Ag-MFI-IE×2	0.159	0.173	0.668	0.000	0.190
AgI-MFI-IE×2-150	0.000	0.000	0.016	0.984	-
Ag-TON-IE×2	0.092	0.171	0.737	0.000	0.101
AgI-TON-IE×2-150	0.017	0.000	0.010	0.974	0.017

valence state of Ag (i.e., Ag^0/Ag^+) can be calculated by assuming that the Ag^+ is contributed by AgI, Ag_2O, and Ag-MOR (i.e., $x_{AgI} + x_{Ag_2O} + x_{Ag-MOR}$), whereas Ag^0 is defined as x_{Ag^0}. The raw data patterns along with the fits are shown in Figure 6. Spectra of Ag-MOR and raw Ag-exchanged samples (without iodine) closely resembled the spectrum of $AgNO_3$. However, based on Raman spectroscopy of these samples (see Figure S13, Supporting Information), it is unlikely that a notable fraction of nitrate was present in the samples before exposure to iodine. However, because of the large overlap between $AgNO_3$ and Ag-MOR, linear combination fitting was performed assuming only Ag-MOR. The lack of features in the Ag K-edge XANES for $AgNO_3$ and Ag-MOR beyond the absorption edge has previously been attributed to the significant positional disorder of Ag, which suppresses spectral features.[60] Similar to Ag-MOR, Ag-exchanged levyne and HZSM-5 zeolites show only broad spectral features in Ag K-edge XANES.[61,62]

The data in Table 2 and Figure 6 show that the sorbents prior to iodine loading contained mostly Ag^+ with some reduced Ag^0 being present, even though no steps were implemented in the procedure to actively reduce the Ag^+ to Ag^0. This has been seen in some of our previous studies using a similar $AgNO_3$ exchange process to incorporate Ag into porous aluminosilicate scaffolds.[13,16,63] These results also show that no Ag^0 is present in AgI-FAU-IE×2-150 or AgI-MFI-IE×2-150 and very little is present in AgI-TON-IE×2-150. Most of the Ag present in the iodine-loaded samples is present as AgI where x_{AgI} = 0.98 for AgI-MFI-IE×2-150 and x_{AgI} = 0.97 for AgI-TON-IE×2-150 but only x_{AgI} = 0.82 for AgI-FAU-IE×2-150. The lower x_{AgI} value for AgI-FAU-IE×2-150 corroborates the lower AgU value (i.e., 0.60; see Table 1) where more Ag was measured with EDS than I, confirming the presence of unreacted and oxidized Ag still present in the zeolite (i.e., reported as Ag-MOR from XANES fitting). In contrast, while the x_{AgI} values for AgI-MFI-IE×2-150 and AgI-TON-IE×2-150 show nearly full utilization of Ag, the AgU values were >1 showing that these sorbents also likely contained physisorbed iodine and/or iodine chemisorbed to other regions of the porous scaffolds (see Table 1 and Figure 5c) as mentioned previously. These types of measurements and analyses are helpful when understanding the Ag utilization (AgU) and oxidation states of the Ag to help with further sorbent development for iodine capture.

The iodine uptake data for the RT experiment are shown in Table 3, and the data as a function of time are shown in Figure 7 for AgI-FAU-IE×2-RT, AgI-MFI-IE×2-RT, and AgI-MOR-RT. The data for AgI-TON-IE×2-RT are not shown due to the erratic nature of the data, which was difficult to interpret and potentially due to water adsorption and desorption with changes in humidity during the experiment. The fluctuations in the AgI-FAU-IE×2-RT and AgI-MFI-IE×2-RT data sets are attributed to changes in moisture in the laboratory over this time period, whereas the AgI-MOR-RT sorbent seemed less affected by this as the data had less scatter, although the relative humidity was not measured during these experiments. For these experiments, the Ag-exchanged (IE×2) zeolites showed some interesting differences compared to those collected at 150 °C. For instance, higher $m_{I,EDS}$ values were seen for FAU of 41.6% (RT) vs 29.0% (150 °C) and lower values were seen for TON of 10.4 (RT) vs 15.0 (150 °C), respectively (see Tables 1, 3, and S3 in the Supporting Information). Interestingly, the values for MFI zeolites were very similar at 8.5 vs 8.4 mass % for RT vs 150 °C experiments, respectively.

The data provided in Figures 5, 7, Tables 1, 3, and Figures S1−S16 (Supporting Information) provide a basis for comparison between the baseline sorbent used by the U.S. Department of Energy (Ag-MOR) for $I_{2(g)}/CH_3I_{(g)}$ and other potential candidate Ag-zeolites like Ag-FAU and Ag-MFI. The data presented in this paper show significant differences in the iodine loading when different zeolites are utilized. The iodine loading data for Ag-FAU (including the IE×1, IE×2, Act-IE×1, and Act-IE×2) all show promise to approximately double the iodine loading from the Ag-MOR baseline sorbent based on some of the data sets. As per Figure 7 alone, the gravimetric changes for the room-temperature iodine loading experiment show a >3× increase in iodine loading of Ag-FAU (IE×2) over that of Ag-MOR (as received).

Figure 8 provides some additional comparisons for the samples including iodine loadings (Figure 8a,c,d), general compositions (Figure 8b), iodine loading versus Ag concentration in the sorbent specifically (Figure 8c), and iodine loading vs the Ag/Al ratio in the sorbent (Figure 8d). Looking at Figure 8a, the data are artificially skewed toward the $m_{I,EDS}$ side of the plot due to the fact that oxygen was not included in the EDS quantification routine due to inaccuracies. Despite this, the MFI zeolites fall very close to the 1:1 (45°) line, suggesting that the MDP values might be artificially inflated for these due to water adsorption during the experiment. Another point of interest here is the fact that the $m_{I,EDS}$ values for AgZ are much higher than those expected based on the MDP values

https://doi.org/10.1021/acsami.2c01179
ACS Appl. Mater. Interfaces 2022, 14, 18439−18452

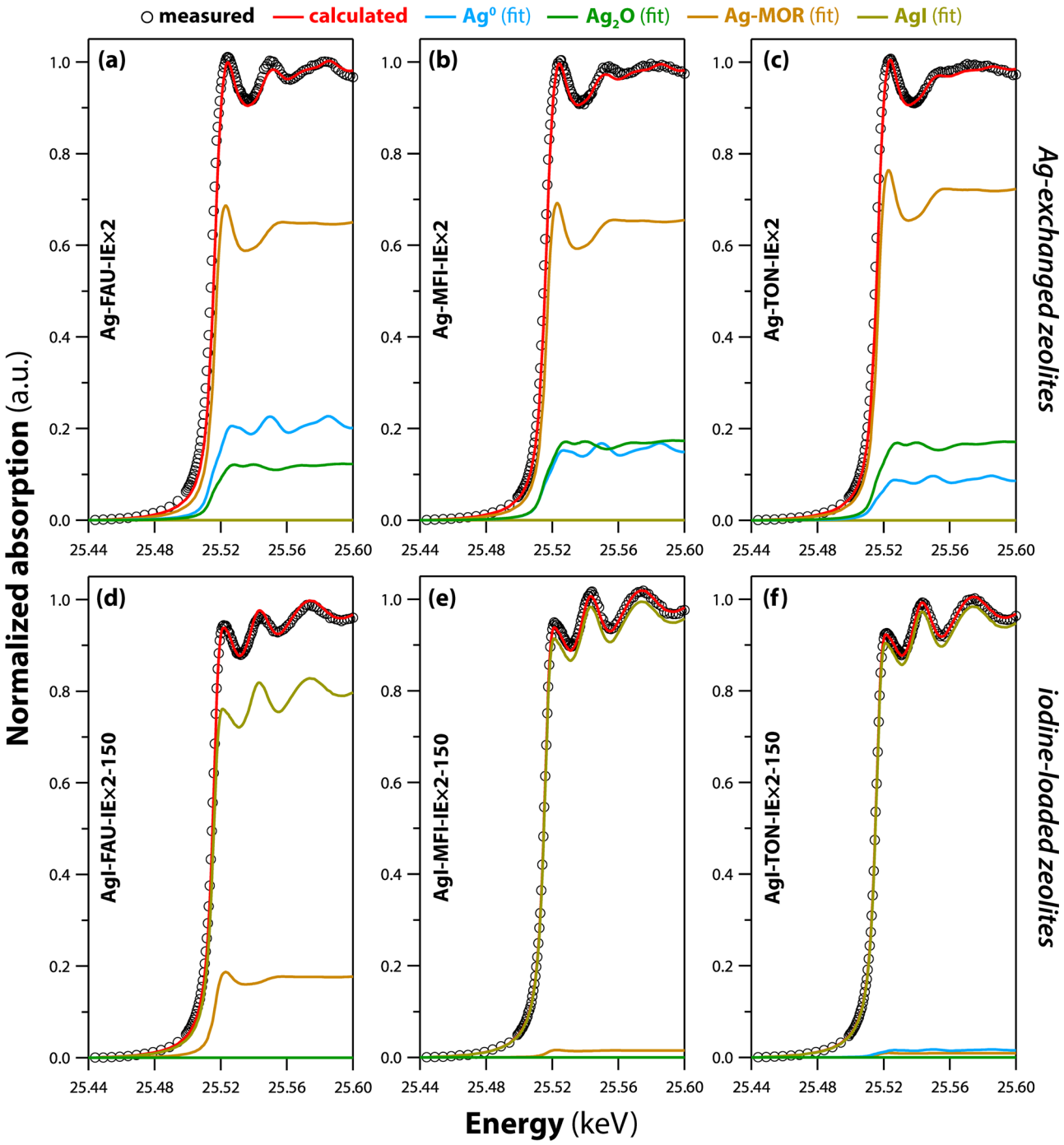

Figure 6. Linear combination fitting visualization for (a) Ag-FAU-IE×2, (b) Ag-MFI-IE×2, (c) Ag-TON-IE×2, (d) AgI-FAU-IE×2-150, (e) AgI-MFI-IE×2-150, and (f) AgI-TON-IE×2-150. Partial spectral contributions were calculated by multiplying molar fractions (x_i) from Table 2 by the normalized XAS data of the corresponding standards. The legend for all spectra is at the top of the figure.

and this could be due to water loss during the experiment resulting in a loss of initial mass ($m_{s,i}$), making the iodine loading values seem lower than they actually are. This discrepancy also supports the need for multiple types of measurements to corroborate data sets for porous sorbents under conditions where water adsorption and desorption could play an important role in tracking iodine capture performance based on mass gain alone. This figure also shows the importance of activating the zeolites before iodine loading as it increased the iodine loading values in nearly every case while these differences were notably higher for FAU zeolites than MFI zeolites. Figure 8b provides the compositions of the zeolites including IE×1 and IE×2 as well as activated IE×1 and IE×2 in addition to Ag-MOR. One of the most important takeaways from Figure 8b is that the Ag concentration did not notably change between the progression of IE×1 → IE×2, showing that the second ion exchange procedure likely did not make any significant improvements. These data also highlight the low Ag concentrations present in the Ag-loaded MFI and TON sorbents. When looking at the $M_{I,EDS}$ as a function of Ag concentrations (Figure 8c) in the sorbents, a general trend is observed where higher Ag concentrations led to higher iodine

https://doi.org/10.1021/acsami.2c01179
ACS Appl. Mater. Interfaces 2022, 14, 18439−18452

Table 3. Mass Uptake and EDS Data for $I_{2(g)}$ Capture of Ag-exchanged (IE×2) Zeolites after Iodine Uptake Experiment at RT[a]

description	sample ID		
	AgI-FAU-IE×2-RT	AgI-MFI-IE×2-RT	AgI-MOR-RT
$m_{s,i}$ (g)	0.0178	0.0286	0.0812
Δm (g)	0.0053	0.0024	0.0082
$100 \times \Delta m/m_{s,f}$ (mass %)	22.90%	7.70%	9.20%
$m_{I,EDS}$ (mass %)	41.6 (0.5)	8.5 (0.7)	22.3 (4.0)
$M_{Ag,EDS}$ (at. %)	19.4 (0.4)	1.8 (0.1)	7.4 (0.9)
$M_{I,EDS}$ (at. %)	21 (0.5)	2.1 (0.2)	7.3 (1.7)
AgU	1.08 (0.02)	1.18 (0.09)	0.98 (0.14)

[a]Data reported here include the initial sample mass (m_s), the mass change during iodine loading (Δm), the mass % change during the experiment ($100 \times \Delta m/m_{s,f}$), the mass % of iodine measured in the sample with EDS (excluding O) ($m_{I,EDS}$), the at. % of Ag measured in the sample with EDS ($M_{Ag,EDS}$), and the at. % of I measured in the sample with EDS ($M_{I,EDS}$). Note that EDS data exclude oxygen and the fact that only unactivated zeolite was studied in these experiments. Values in parenthesis are standard deviations ($\pm 1\sigma$) from multiple measurements.

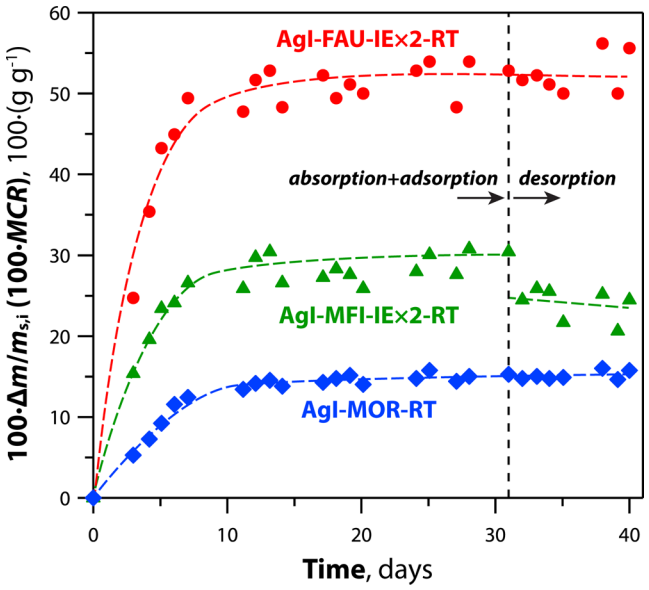

Figure 7. Summary of $I_{2(g)}$ uptake at room temperature of AgI-FAU-IE×2-RT, AgI-MFI-IE×2-RT, and Ag-MOR-RT. The data to the left of the vertical dotted line show absorption + adsorption and those to the right signify those under desorption (i.e., after the iodine was removed from the sample container). Dashed lines are drawn on top of the data as a guide to the eye (these are not calculated trendlines).

concentrations in the final sorbent. Because the Ag concentrations of the MFI and TON zeolites were so similar, the trend visualization is not as clear as when these Ag concentrations were spread out over a wider range.

When looking at the $M_{I,EDS}$ as a function of Ag/Al ratios (Figure 8d), the MFI and TON zeolites show a somewhat linear trend, but the Ag-MOR and Ag-FAU zeolites are not part of that trend and are seen much higher on the plot. Thus, while the presence of Ag in the sorbent is directly related to the performance of the sorbent during iodine capture, it is likely not the only parameter that is important to maximize these loadings.

Comparing the performance of the Ag-FAU with other iodine sorbents, zeolites fall well below some of the top performers that can capture upward of 2 g g^{-1} of iodine such as MOFs,[6,64,65] COFs,[66] and chalcogenide aerogels,[67,68] most of which tend to capture iodine via physisorption over chemisorption. They also fall short of pure metal substrates such as Cu^0 (0.712 g g^{-1}), Ag^0 (1.19 g g^{-1}), In^0 (3.34 g g^{-1}), and Sn^0 (4.37 g g^{-1}).[69] Despite this discrepancy, a benefit of using zeolites for this application is that they are more mechanically robust materials and overall inexpensive for implementation in an industrial facility but also tend to chemisorb iodine to form metal iodides (e.g., as AgI) rather than physisorb iodine like many top-performing iodine sorbents; chemisorption leads to a more stable configuration for long-term storage of iodine after capturing than physisorption. Sorbents such as aerogels and xerogels tend to have lower mechanical integrity (and higher specific surface areas) than clay-bound zeolite particles. Based on the EDS data presented herein, Ag-FAU materials in the current study are close in iodine loadings to other porous Ag-aluminosilicate sorbents in the form of aerogels and xerogels from our previous work.[13,16,45,63] Comparisons between the best-performing zeolite sorbent in this study with some other iodine sorbents from the literature are provided in Table S5 (Ag-based sorbents) and Table S6 (non-Ag sorbents) (Supporting Information). One key difference between the performance of the Ag-FAU sorbents and those from our previous work is that the AgU values for the Ag-FAU sorbents are in the range of 0.60−0.90, whereas those of the Ag-aluminosilicate gels are typically higher than 1 (i.e., 0.87−1.20);[16,45,63] note that AgU values >1 denote that some of the iodine is chemisorbing to a site alternative to the Ag or some physisorbed iodine likely exists within the porous microstructure. These types of comparisons are helpful when selecting iodine sorbents for different environments such as those with different humidities, different temperatures, and other types of contaminants where selective reactivities might be needed (e.g., in the presence of other halides).

CONCLUSIONS

Because various isotopes and species of iodine can be released during used nuclear fuel reprocessing and nuclear accidents, effective sorbents are needed to capture these species before they are released into the environment. In this work, eight different types of sorbents (i.e., zeolites and mesoporous substrates) were evaluated for $I_{2(g)}$ capture from sublimed vapors of iodine crystals at 150 °C. From this scoping study, four different Ag-exchanged zeolites were investigated (i.e., Ag-FAU, Ag-MFI, and Ag-TON) further in addition to the U.S. Department of Energy baseline iodine sorbent (i.e., Ag-MOR). Of these, the Ag-FAU had the highest uptake of iodine at both room temperature and at 150 °C with over double (nearly triple) the iodine loading of the Ag-MOR. These results were achieved with Ag-zeolites where the Ag was not actively

https://doi.org/10.1021/acsami.2c01179
ACS Appl. Mater. Interfaces 2022, 14, 18439−18452

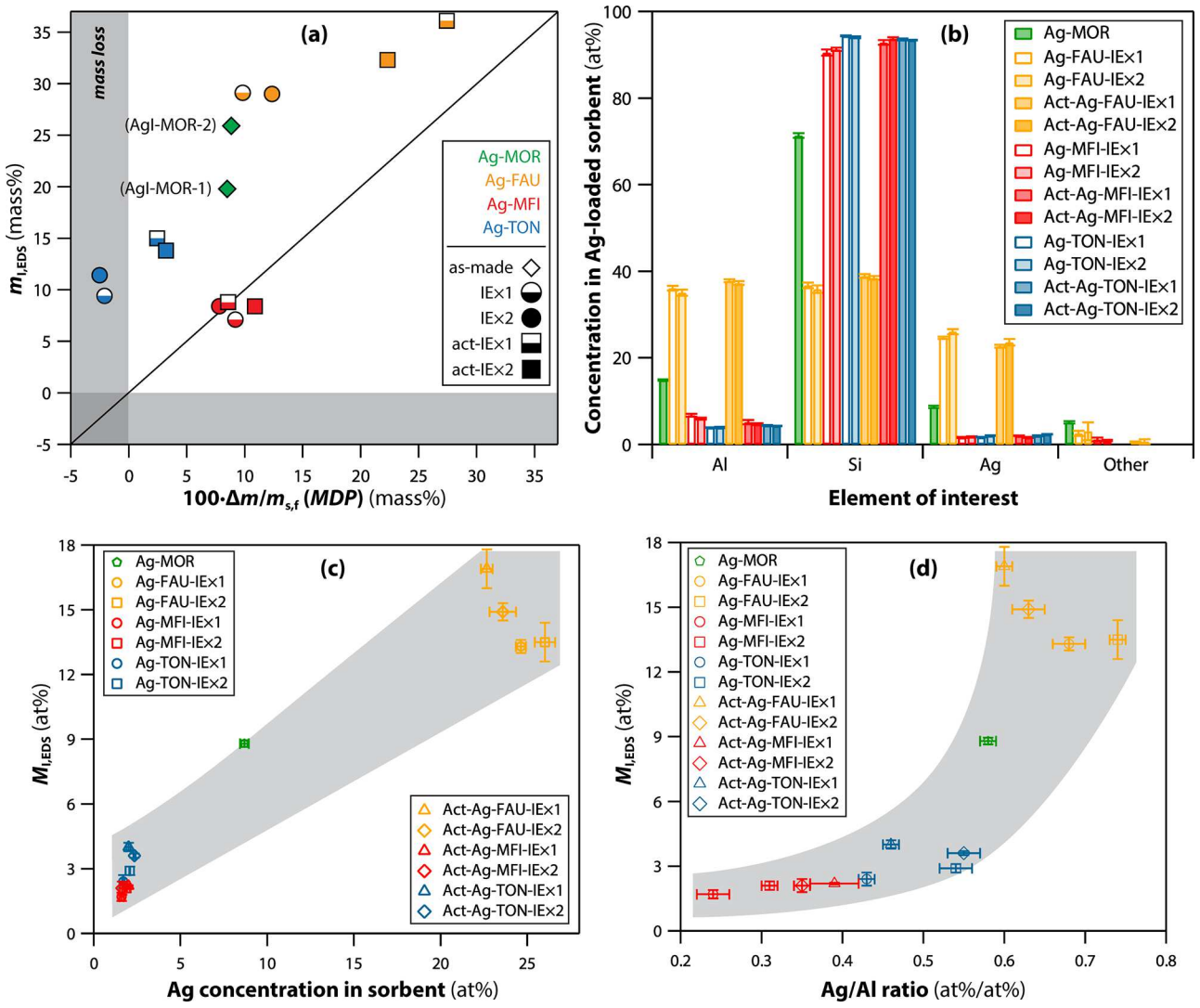

Figure 8. (a) Comparison of $m_{I,EDS}$ vs MDP for the IEx1, IEx2, act-IEx1, act-IEx2 Ag-FAU, Ag-MFI, and Ag-TON zeolites in addition to as-received Ag-MOR (IONEX Ag-900). Note that "act" denotes activated samples. Here, the $m_{I,EDS}$ data exclude oxygen for quantification so these data are already artificially inflated based on actual iodine concentrations in the iodine-loaded samples. Values in the gray region denote mass loss. (b) Compositions of various zeolite sorbents used in this study at different stages; no notable improvements were observed in the Ag-loading between IEx1 and IEx2 steps. (c) $M_{I,EDS}$ vs Ag concentration in the sorbents [from (b)], and (d) $M_{I,EDS}$ vs the Ag/Al molar ratio in the sorbent. For (c,d), gray regions show the general data trends as a guide to the eye. Iodine loading data is from Table 1 (for 150 °C loading temperature) and compositions are from Table S3 (Supporting Information).

reduced, so it is possible that even higher iodine loadings and Ag-utilization values could be achieved.

The P-XRD analysis of iodine-loaded sorbents showed AgI formation (β and γ forms) for MFI and FAU zeolites with some inconclusive results for the TON zeolites. While the FAU zeolites showed the highest iodine capacities, the FAU zeolite structure broke down during the iodine-loading experiment at 150 °C, whereas this was not the case for the MFI and TON zeolites. The SEM analyses show distinct crystallite sizes and shapes for the different zeolites but with different morphologies, as expected. The XANES analyses revealed mixtures of Ag^0 and Ag^+ species present in the IEx2 FAU, MFI, and TON samples (highest Ag^0 was for Ag-FAU and lowest was for Ag-TON) where the majority Ag-based phase was AgI after iodine capture. These types of measurements and analyses are helpful for selecting Ag-containing iodine capture media for different applications.

■ ASSOCIATED CONTENT

Supporting Information

The Supporting Information is available free of charge at https://pubs.acs.org/doi/10.1021/acsami.2c01179.

Detailed materials and methods including base sample synthesis, iodine loading of base sorbents (without Ag), pictures, P-XRD data, SEM data, XAS data, Raman methods and data, EDS data, room-temperature iodine loading data for Ag-TON, and comparisons of iodine capture data with literature values (PDF)

■ AUTHOR INFORMATION

Corresponding Authors

Brian J. Riley − *Energy and Environment Directorate, Pacific Northwest National Laboratory, Richland, Washington 99352, United States;* orcid.org/0000-0002-7745-6730; Email: brian.riley@pnnl.gov

https://doi.org/10.1021/acsami.2c01179
ACS Appl. Mater. Interfaces 2022, 14, 18439−18452

Miroslaw A. Derewinski − *Jerzy Haber Institute of Catalysis and Surface Chemistry, Polish Academy of Sciences, 30-239 Cracow, Poland;* orcid.org/0000-0003-1738-2247; Email: ncderewi@cyf-kr.edu.pl

Radha Kishan Motkuri − *Energy and Environment Directorate, Pacific Northwest National Laboratory, Richland, Washington 99352, United States;* orcid.org/0000-0002-2079-4798; Email: radhakishan.motkuri@pnnl.gov

Authors

Saehwa Chong − *Energy and Environment Directorate, Pacific Northwest National Laboratory, Richland, Washington 99352, United States;* orcid.org/0000-0002-4722-0022

Julian Schmid − *Physical and Computational Sciences Directorate, Pacific Northwest National Laboratory, Richland, Washington 99352, United States*

José Marcial − *Energy and Environment Directorate, Pacific Northwest National Laboratory, Richland, Washington 99352, United States*

Emily T. Nienhuis − *Energy and Environment Directorate, Pacific Northwest National Laboratory, Richland, Washington 99352, United States*

Mrinal K. Bera − *NSF's ChemMatCARS, Pritzker School of Molecular Engineering, University of Chicago, Chicago, Illinois 60637, United States;* orcid.org/0000-0003-0698-5253

Sungsik Lee − *X-Ray Science Division, Argonne National Laboratory, Lemont, Illinois 60439, United States;* orcid.org/0000-0002-1425-9852

Nathan L. Canfield − *Energy and Environment Directorate, Pacific Northwest National Laboratory, Richland, Washington 99352, United States*

Sungmin Kim − *Physical and Computational Sciences Directorate, Pacific Northwest National Laboratory, Richland, Washington 99352, United States;* orcid.org/0000-0001-6602-1320

Complete contact information is available at: https://pubs.acs.org/10.1021/acsami.2c01179

Notes

The authors declare no competing financial interest.

■ ACKNOWLEDGMENTS

Pacific Northwest National Laboratory (PNNL) is operated by Battelle Memorial Institute for the DOE under contract DE-AC05-76RL01830. Raman spectroscopy was performed using facilities at the Environmental Molecular Science Laboratory (EMSL, grid.436923.9), a DOE Office of Science User Facility sponsored by the Office of Biological and Environmental Research at Pacific Northwest National Laboratory (PNNL). The authors are thankful to Ken Marsden and James King at Idaho National Laboratory for programatic support, Jacob Peterson (PNNL) for help with initial experiments on the base zeolites, Josef Matyas (PNNL) for help with the iodine loading of the base materials, and Carter Abney and Georgia Cametti for sharing measured XANES data of Ag-mordenite and Ag-levyne. This work was funded by the Department of Energy Office of Nuclear Energy. This research used the Advanced Photon Source resources, a U.S. Department of Energy (DOE) Office of Science User Facility, operated for the DOE Office of Science by Argonne National Laboratory under Contract no. DE-AC02-06CH11357. In this research, some of the experiments were performed at NSF's ChemMatCARS, which is supported by the Divisions of Chemistry (CHE) and Materials Research (DMR), National Science Foundation, under grant number NSF/CHE-1834750. Extraordinary facility operations were supported in part by the DOE Office of Science through the National Virtual Biotechnology Laboratory, a consortium of DOE national laboratories focused on the response to COVID-19, with funding provided by the Coronavirus CARES Act.

■ REFERENCES

(1) Riley, B. J.; Vienna, J. D.; Strachan, D. M.; McCloy, J. S.; Jerden, J. L. Materials and Processes for the Effective Capture and Immobilization of Radioiodine: A Review. *J. Nucl. Mater.* **2016**, *470*, 307−326.

(2) Lebel, L. S.; Dickson, R. S.; Glowa, G. A. Radioiodine in the Atmosphere After the Fukushima Dai-ichi Nuclear Accident. *J. Environ. Radioact.* **2016**, *151*, 82−93.

(3) Zablotska, L. B.; Ron, E.; Rozhko, A. V.; Hatch, M.; Polyanskaya, O. N.; Brenner, A. V.; Lubin, J.; Romanov, G. N.; McConnell, R. J.; O'Kane, P.; Evseenko, V. V.; Drozdovitch, V. V.; Luckyanov, N.; Minenko, V. F.; Bouville, A.; Masyakin, V. B. Thyroid Cancer Risk in Belarus Among Children and Adolescents Exposed to Radioiodine After the Chornobyl Accident. *Br. J. Cancer* **2011**, *104*, 181−187.

(4) Tokonami, S.; Hosoda, M.; Akiba, S.; Sorimachi, A.; Kashiwakura, I.; Balonov, M. Thyroid Doses for Evacuees from the Fukushima Nuclear Accident. *Sci. Rep.* **2012**, *2*, 507.

(5) Banerjee, D.; Chen, X.; Lobanov, S. S.; Plonka, A. M.; Chan, X.; Daly, J. A.; Kim, T.; Thallapally, P. K.; Parise, J. B. Iodine Adsorption in Metal Organic Frameworks in the Presence of Humidity. *ACS Appl. Mater. Interfaces* **2018**, *10*, 10622−10626.

(6) Sava, D. F.; Rodriguez, M. A.; Chapman, K. W.; Chupas, P. J.; Greathouse, J. A.; Crozier, P. S.; Nenoff, T. M. Capture of Volatile Iodine, a Gaseous Fission Product, by Zeolitic Imidazolate Framework-8. *J. Am. Chem. Soc.* **2011**, *133*, 12398−12401.

(7) Li, J.; Zhang, H.; Zhang, L.; Wang, K.; Wang, Z.; Liu, G.; Zhao, Y.; Zeng, Y. Two-Dimensional Covalent−Organic Frameworks for Ultrahigh Iodine Capture. *J. Mater. Chem. A* **2020**, *8*, 9523−9527.

(8) Azambre, B.; Chebbi, M.; Ibrahim, N. Structure-Activity Relationships between the State of Silver on Different Supports and Their I_2 and CH_3I Adsorption Properties. *Nanomaterials* **2021**, *11*, 11.

(9) Azambre, B.; Chebbi, M. Evaluation of Silver Zeolites Sorbents Toward Their Ability to Promote Stable CH_3I Storage as AgI Precipitates. *ACS Appl. Mater. Interfaces* **2017**, *9*, 25194−25203.

(10) Yan, Z.; Yuan, Y.; Tian, Y.; Zhang, D.; Zhu, G. Highly Efficient Enrichment of Volatile Iodine by Charged Porous Aromatic Frameworks with Three Sorption Sites. *Angew. Chem., Int. Ed.* **2015**, *54*, 12733−12737.

(11) Al-Mamoori, A.; Alsalbokh, M.; Lawson, S.; Rownaghi, A. A.; Rezaei, F. Development of Bismuth-Mordenite Adsorbents for Iodine Capture from Off-Gas Streams. *Chem. Eng. J.* **2020**, *391*, 123583.

(12) Yang, J. H.; Cho, Y.-J.; Shin, J. M.; Yim, M.-S. Bismuth-Embedded SBA-15 Mesoporous Silica for Radioactive Iodine Capture and Stable Storage. *J. Nucl. Mater.* **2015**, *465*, 556−564.

(13) Riley, B. J.; Kroll, J. O.; Peterson, J. A.; Matyáš, J.; Olszta, M. J.; Li, X.; Vienna, J. D. Silver-Loaded Aluminosilicate Aerogels as Iodine Sorbents. *ACS Appl. Mater. Interfaces* **2017**, *9*, 32907−32919.

(14) Matyáš, J.; Ilton, E. S.; Kovařík, L. Silver-Functionalized Silica Aerogel: Towards an Understanding of Aging on Iodine Sorption Performance. *RSC Adv.* **2018**, *8*, 31843−31852.

(15) Matyas, J.; Ilton, E. S.; Lahiri, N.; Li, X. S.; Silverstein, J. A. *Bismuth-Functionalized Silica Aerogels for Iodine Capture, PNNL-32086*; Pacific Northwest National Laboratory, 2021.

(16) Chong, S.; Riley, B. J.; Kuang, W.; Olszta, M. J. Iodine Capture with Mechanically Robust Heat-Treated Ag-Al-Si-O Xerogel Sorbents. *ACS Omega* **2021**, *6*, 11628−11638.

(17) Tian, Z.; Chee, T.-S.; Zhu, L.; Duan, T.; Zhang, X.; Lei, L.; Xiao, C. Comprehensive Comparison of Bismuth and Silver

Functionalized Nickel Foam Composites in Capturing Radioactive Gaseous Iodine. *J. Hazard Mater.* **2021**, *417*, 125978.
(18) Yang, J. H.; Shin, J. M.; Park, J. J.; Park, G. I.; Yim, M. S. Novel Synthesis of Bismuth-Based Adsorbents for the Removal of ^{129}I in Off-Gas. *J. Nucl. Mater.* **2015**, *457*, 1−8.
(19) Barpaga, D.; Zheng, J.; McGrail, B. P.; Motkuri, R. K. Manipulating Pore Topology and Functionality to Promote Fluorocarbon-Based Adsorption Cooling. *Acc. Chem. Res.* **2022**, *55*, 649−659.
(20) Zheng, J.; Wahiduzzaman, M.; Barpaga, D.; Trump, B. A.; Gutiérrez, O. Y.; Thallapally, P.; Ma, S.; McGrail, B. P.; Maurin, G.; Motkuri, R. K. Porous Covalent Organic Polymers for Efficient Fluorocarbon-Based Adsorption Cooling. *Angew. Chem., Int. Ed.* **2021**, *60*, 18037−18043.
(21) Oleksiak, M. D.; Ghorbanpour, A.; Conato, M. T.; McGrail, B. P.; Grabow, L. C.; Motkuri, R. K.; Rimer, J. D. Synthesis Strategies for Ultrastable Zeolite GIS Polymorphs as Sorbents for Selective Separations. *Chem.—Eur. J.* **2016**, *22*, 16078−16088.
(22) Che, S.; Pang, J.; Kalin, A. J.; Wang, C.; Ji, X.; Lee, J.; Cole, D.; Li, J.-L.; Tu, X.; Zhang, Q.; Zhou, H.-C.; Fang, L. Rigid Ladder-Type Porous Polymer Networks for Entropically Favorable Gas Adsorption. *ACS Mater. Lett.* **2020**, *2*, 49−54.
(23) Zheng, J.; Barpaga, D.; Trump, B. A.; Shetty, M.; Fan, Y.; Bhattacharya, P.; Jenks, J. J.; Su, C.-Y.; Brown, C. M.; Maurin, G.; McGrail, B. P.; Motkuri, R. K. Molecular Insight into Fluorocarbon Adsorption in Pore Expanded Metal-Organic Framework Analogs. *J. Am. Chem. Soc.* **2020**, *142*, 3002−3012.
(24) Zheng, J.; Vemuri, R. S.; Estevez, L.; Koech, P. K.; Varga, T.; Camaioni, D. M.; Blake, T. A.; McGrail, B. P.; Motkuri, R. K. Pore-Engineered Metal-Organic Frameworks with Excellent Adsorption of Water and Fluorocarbon Refrigerant for Cooling Applications. *J. Am. Chem. Soc.* **2017**, *139*, 10601−10604.
(25) Estevez, L.; Barpaga, D.; Zheng, J.; Sabale, S.; Patel, R. L.; Zhang, J.-G.; McGrail, B. P.; Motkuri, R. K. Hierarchically Porous Carbon Materials for CO_2 Capture: The Role of Pore Structure. *Ind. Eng. Chem. Res.* **2018**, *57*, 1262−1268.
(26) Baerlocher, C.; McCusker, L. B.; Olson, D. H. *Atlas of Zeolite Framework Types*, 6th revised ed.; Elsevier: Oxford, 2007.
(27) Riley, B. J.; Chong, S. Crystalline Aluminosilicates for Radionuclide Remediation. In *An Introduction to Aluminosilicates*; Blevins, N. R., Ed.; Nova Science Publishers, 2020.
(28) Degnan, T. F. Applications of Zeolites in Petroleum Refining. *Top. Catal.* **2000**, *13*, 349−356.
(29) Bower, J. K.; Barpaga, D.; Prodinger, S.; Krishna, R.; Schaef, H. T.; McGrail, B. P.; Derewinski, M. A.; Motkuri, R. K. Dynamic adsorption of CO_2/N_2 on cation-exchanged chabazite SSZ-13: A breakthrough analysis. *ACS Appl. Mater. Interfaces* **2018**, *10*, 14287−14291.
(30) Prodinger, S.; Vemuri, R. S.; Varga, T.; Peter McGrail, B.; Motkuri, R. K.; Derewinski, M. A. Impact of Chabazite SSZ-13 Textural Properties and Chemical Composition on CO_2 Adsorption Applications. *New J. Chem.* **2016**, *40*, 4375−4385.
(31) Chong, S.; Peterson, J.; Nam, J.; Riley, B.; McCloy, J. Synthesis and Characterization of Iodosodalite. *J. Am. Ceram. Soc.* **2017**, *100*, 2273−2284.
(32) Chong, S.; Peterson, J. A.; Riley, B. J.; Tabada, D.; Wall, D.; Corkhill, C. L.; McCloy, J. S. Glass-Bonded Iodosodalite Waste Form for Immobilization of ^{129}I. *J. Nucl. Mater.* **2018**, *504*, 109−121.
(33) Maddrell, E. R.; Vance, E. R.; Gregg, D. J. Capture of Iodine from the Vapour Phase and Immobilisation as Sodalite. *J. Nucl. Mater.* **2015**, *467*, 271−279.
(34) Chebbi, M.; Chibani, S.; Paul, J.-F.; Cantrel, L.; Badawi, M. Evaluation of Volatile Iodine Trapping in Presence of Contaminants: A Periodic DFT Study on Cation Exchanged-Faujasite. *Microporous Mesoporous Mater.* **2017**, *239*, 111−122.
(35) Riley, B. J.; Vienna, J. D.; Frank, S. M.; Kroll, J. O.; Peterson, J. A.; Canfield, N. L.; Zhu, Z.; Zhang, J.; Kruska, K.; Schreiber, D. K.; Crum, J. V. Glass Binder Development for a Glass-Bonded Sodalite Ceramic Waste Form. *J. Nucl. Mater.* **2017**, *489*, 42−63.
(36) Garn, T. G.; Greenhalgh, M.; Law, J. D. Development and Evaluation of a Silver Mordenite Composite Sorbent for the Partitioning of Xenon from Krypton in Gas Compositions. *J. Nucl. Sci. Technol.* **2015**, *53*, 1484−1488.
(37) Thomas, T. R.; Murphy, L. P.; Staples, B. A.; Nichols, J. T. *Airborne Elemental Iodine Loading Capacities of Metal Zeolites and a Method for Recycling Silver Zeolite, ICP-1119*; Idaho National Laboratory, 1977.
(38) Sheppard, G. P.; Hriljac, J. A.; Maddrell, E. R.; Hyatt, N. C. Silver Zeolites: Iodide Occlusion and Conversion to Sodalite - A Potential 129I Waste Form? *MRS Online Proc. Libr.* **2006**, *932*, 361.
(39) Bruffey, S. H.; Jubin, R. T.; Jordan, J. A. *Fundamental Aspects of Zeolite Waste Form Production by Hot Isostatic Pressing, FCRD-MRWFD-2016-000267, ORNL/SR-2016/759*; Oak Ridge National Laboratory, 2016.
(40) Chapman, K. W.; Chupas, P. J.; Nenoff, T. M. Radioactive Iodine Capture in Silver-Containing Mordenites Through Nanoscale Silver Iodide Formation. *J. Am. Chem. Soc.* **2010**, *132*, 8897−8899.
(41) Nan, Y.; Tavlarides, L. L.; DePaoli, D. W. Adsorption of Iodine on Hydrogen-Reduced Silver-Exchanged Mordenite: Experiments and Modeling. *AIChE J.* **2016**, *63*, 1024−1035.
(42) Jubin, R. T. *A Literature Survey of Methods to Remove Iodine from off-Gas Streams Using Solid Sorbents, ORNL/TM-6607*; Oak Ridge National Laboratory, 1979.
(43) Pankratz, L. B. *Thermodynamic Properties of Elements and Oxides*; U.S. Department of the Interior, Bureau of Mines: Washington, D.C., 1982; Vol. *672*.
(44) Pankratz, L. B. *Thermodynamic Properties of Halides*; U.S. Department of the Interior, Bureau of Mines: Washington, D.C., 1984; Vol. *674*.
(45) Riley, B. J.; Chong, S.; Olszta, M. J.; Peterson, J. A. Evaluation of Getter Metals in Na-Al-Si-O Aerogels and Xerogels for the Capture of Iodine Gas. *ACS Appl. Mater. Interfaces* **2020**, *12*, 19682−19692.
(46) Maeck, W. J.; Pence, D. T.; Keller, J. H. *A Highly Efficient Inorganic Adsorber for Airborne Iodine Species (Silver Zeolite Development Studies), IN-1224*; Idaho Nuclear Corporation - National Reactor Testing Station, 1968.
(47) Hersh, C. K. *Molecular Sieves*; Reinhold Publishing Company: New York, NY, 1961.
(48) Pence, D. T.; Duce, F. A.; Maeck, W. J. *In 12th AEC Air Cleaning Conference, CONF 720823; Developments in the Removal of Airborne Iodine Species with Metal Substituted Zeolites Oak Ridge, TN*, 1972; p 417.
(49) Yang, S.; Navrotsky, A.; Phillips, B. L. An In Situ Calorimetric Study of the Synthesis of FAU Zeolite. *Microporous Mesoporous Mater.* **2001**, *46*, 137−151.
(50) Prodinger, S.; Vjunov, A.; Hu, J. Z.; Fulton, J. L.; Camaioni, D. M.; Derewinski, M. A.; Lercher, J. A. Elementary Steps of Faujasite Formation Followed by In Situ Spectroscopy. *Chem. Mater.* **2018**, *30*, 888−897.
(51) Liang, T.; Chen, J.; Qin, Z.; Li, J.; Wang, P.; Wang, S.; Wang, G.; Dong, M.; Fan, W.; Wang, J. Conversion of Methanol to Olefins Over H-ZSM-5 Zeolite: Reaction Pathway Is Related to the Framework Aluminum Siting. *ACS Catal.* **2016**, *6*, 7311−7325.
(52) Wang, Y.; Song, J.; Baxter, N. C.; Kuo, G.-T.; Wang, S. Synthesis of Hierarchical ZSM-5 Zeolites by Solid-State Crystallization and their Catalytic Properties. *J. Catal.* **2017**, *349*, 53−65.
(53) Derewinski, M.; Sarv, P.; Mifsud, A. Thermal Stability and Siting of Aluminum in Isostructural ZSM-22 and Theta-1 Zeolites. *Catal. Today* **2006**, *114*, 197−204.
(54) Kumar, R.; Ratnasamy, P. Isomerization and Formation of Xylenes over ZSM-22 and ZSM-23 zeolites. *J. Catal.* **1989**, *116*, 440−448.
(55) Zhao, D.; Huo, Q.; Feng, J.; Chmelka, B. F.; Stucky, G. D. Nonionic Triblock and Star Diblock Copolymer and Oligomeric Surfactant Syntheses of Highly Ordered, Hydrothermally Stable, Mesoporous Silica Structures. *J. Am. Chem. Soc.* **1998**, *120*, 6024−6036.

https://doi.org/10.1021/acsami.2c01179
ACS Appl. Mater. Interfaces 2022, 14, 18439−18452

(56) Pashkova, V.; Włoch, E.; Mikołajczyk, A.; Łaniecki, M.; Sulikowski, B.; Derewiński, M. Composite SBA-15/MFI Type Materials: Preparation, Characterization and Catalytic Performance. *Catal. Lett.* **2009**, *128*, 64−71.
(57) Cheary, R. W.; Coelho, A. A.; Cline, J. P. Fundamental Parameters Line Profile Fitting in Laboratory Diffractometers. *J. Res. Natl. Inst. Stand. Technol.* **2004**, *109*, 1−25.
(58) Ravel, B.; Newville, M. ATHENA, ARTEMIS, HEPHAESTUS: Data Analysis for X-ray Absorption Spectroscopy Using IFEFFIT. *J. Synchrotron Radiat.* **2005**, *12*, 537−541.
(59) Xian, Q.; Chen, L.; Fan, W.; Liu, Y.; He, X.; Dan, H.; Zhu, L.; Ding, Y.; Duan, T. Facile Synthesis of Novel Bi^0-SBA-15 Adsorbents by an Improved Impregnation Reduction Method for Highly Efficient Capture of Iodine Gas. *J. Hazard Mater.* **2022**, *424*, 127678.
(60) Abney, C. W.; Nan, Y.; Tavlarides, L. L. X-Ray Absorption Spectroscopy Investigation of Iodine Capture by Silver-Exchanged Mordenite. *Ind. Eng. Chem. Res.* **2017**, *56*, 4837−4846.
(61) Ruan, H.; Nishibori, M.; Uchiyama, T.; Ninomiya, K.; Kamitani, K.; Kato, K.; Konishi, Y.; Haensch, A.; Barsan, N.; Weimar, U.; Shimanoe, K. Soot Oxidation Performance with a HZSM-5 Supported Ag Nanoparticles Catalyst and the Characterization of Ag Species. *RSC Adv.* **2017**, *7*, 43789−43797.
(62) Cametti, G.; Scheinost, A. C.; Churakov, S. V. Structural Evolution of Ag-LEV Zeolite Upon Heating: An In Situ Single-Crystal X-ray Diffraction (SC-XRD) and X-Ray Absorption Spectroscopy (XAS) Study. *ACS Omega* **2020**, *5*, 31774−31783.
(63) Chong, S.; Riley, B. J.; Peterson, J. A.; Olszta, M. J.; Nelson, Z. J. Gaseous Iodine Sorbents: A Comparison Between Ag-Loaded Aerogel and Xerogel Scaffolds. *ACS Appl. Mater. Interfaces* **2020**, *12*, 26127−26136.
(64) Sava, D. F.; Chapman, K. W.; Rodriguez, M. A.; Greathouse, J. A.; Crozier, P. S.; Zhao, H.; Chupas, P. J.; Nenoff, T. M. Competitive I_2 Sorption by Cu-BTC from Humid Gas Streams. *J. Am. Chem. Soc.* **2013**, *25*, 2591−2596.
(65) Chen, P.; He, X.; Pang, M.; Dong, X.; Zhao, S.; Zhang, W. Iodine Capture Using Zr-Based Metal−Organic Frameworks (Zr-MOFs): Adsorption Performance and Mechanism. *ACS Appl. Mater. Interfaces* **2020**, *12*, 20429−20439.
(66) Wang, P.; Xu, Q.; Li, Z.; Jiang, W.; Jiang, Q.; Jiang, D. Exceptional Iodine Capture in 2D Covalent Organic Frameworks. *Adv. Mater.* **2018**, *30*, 1801991.
(67) Riley, B. J.; Chun, J.; Um, W.; Lepry, W. C.; Matyas, J.; Olszta, M. J.; Li, X.; Polychronopoulou, K.; Kanatzidis, M. G. Chalcogen-Based Aerogels As Sorbents for Radionuclide Remediation. *Environ. Sci. Technol.* **2013**, *47*, 7540−7547.
(68) Subrahmanyam, K. S.; Sarma, D.; Malliakas, C. D.; Polychronopoulou, K.; Riley, B. J.; Pierce, D. A.; Chun, J.; Kanatzidis, M. G. Chalcogenide Aerogels as Sorbents for Radioactive Iodine. *Chem. Mater.* **2015**, *27*, 2619−2626.
(69) Riley, B. J.; Chong, S.; Beck, C. L. Iodine Vapor Reactions with Pure Metal Wires at Temperatures of 100-139°C in Air. *Ind. Eng. Chem. Res.* **2021**, *60*, 17162−17173.

https://doi.org/10.1021/acsami.2c01179
ACS Appl. Mater. Interfaces 2022, 14, 18439−18452